Materials Advances

ROYAL SOCIETY OF CHEMISTRY

PAPER

View Article Online
View Journal | View Issue

Cite this: *Mater. Adv.*, 2024, 5, 4865

$MgIn_2S_4$-decorated MOF-derived C/N–CeO_2 nanorod heterojunctions as efficient photocatalysts towards H_2O_2 production reactions and H_2 evolution reactions†

Jayashree Panda, Pragyandeepti Behera, Satyabrata Subudhi, Suraj Prakash Tripathy, Gayatri Swain, Srabani Dash and Kulamani Parida *

Received 15th March 2024,
Accepted 13th April 2024

DOI: 10.1039/d4ma00271g

rsc.li/materials-advances

The design of defect-induced metal oxide–based photocatalysts with precise reactive sites, facilitating photogenerated charge migration, and strong visible light harvesting capacity is not straightforward. Herein, Ce-MOF and $MgIn_2S_4$ (MIS) were used as precursor materials to prepare hierarchical C/N–CeO_2/MIS, 1D–2D heterostructures using a facile *in situ* hydrothermal technique. Among all the heterojunction composites, 20 wt% MIS-decorated C/N–CeO_2 (MC-2) nanohybrids displayed the highest H_2O_2 and H_2 evolution rates (2520.4 μmol h^{-1} g^{-1} and 419.2 μmol h^{-1}) with conversion efficiencies of 0.11% and 6.73%, respectively. A higher Ce(III) atomic fraction and more oxygen vacancies on the surface of MC-2 were shown by X-ray photoelectron spectroscopy (XPS), Raman spectroscopy, and electron paramagnetic resonance (EPR) study. In addition, HRTEM and surface charge analysis confirm the robust interfacial interaction between C/N–CeO_2 and MIS. The mechanism of charge transfer and separation within the *Z*-scheme heterojunction was studied by ultraviolet photoelectron spectroscopy (UPS) and electron spin resonance (ESR) spectroscopy. This research opens up a new avenue for the rational design of inexpensive MOF-derived metal oxide–based photocatalysts for various photocatalytic applications.

1. Introduction

Hydrogen peroxide (H_2O_2) is a flexible and environmentally friendly oxidizing agent used in a wide array of fields such as disinfection, chemical industries, and environmental cleanup. Visible light–driven H_2O_2 production and water reduction reactions comprise a promising strategy for the generation of environmentally friendly oxidants and clean fuels.[1] Since Thenard produced H_2O_2 for the first time in 1818 by reacting barium peroxide with nitric acid, the compound has received increasing attention over the last 200 years.[2] Among the numerous approaches including electrolysis of aqueous H_2SO_4, electrochemical reaction of H_2O and O_2, and sequential reduction and oxidation of an alkyl anthraquinone, the photocatalytic technique is the most globally friendly and sustainable method for producing H_2O_2, as it avoids complicated industrial routes, toxic by-products, and high cost.[3] Nevertheless, the shortage of fossil fuels and environmental disquiet due to our changing world stimulated the research group to search for green substitutes for energy carrier routes. In this context, photon energy–mediated water splitting to generate H_2 gas can be a sustainable alternative to non-renewable energy resources for tackling the global issues of climate crisis and pollution. At the same time, the generation of O_2 significantly contributes to photoelectrochemical water splitting and artificial photosynthesis. Therefore, photocatalytic H_2O_2 production and water splitting have recently gained global interest among all the domains of materials scientists for exploring a safer, more efficient, green, and low-cost synthesis pathway.

Among the various potential semiconducting materials, metal organic frameworks (MOFs), a class of coordination polymer, have attracted significant attention due to their advantageous properties such as designable pore structure, high surface areas, free volume, and low density.[4–6] Besides, these ultra-stable frameworks used in catalysis, gas sensing, supercapacitors, *etc.*, can act as potential precursors for doped metal oxide synthesis.[7–9] The superiority of these MOF-derived metal oxides over their conventional counterparts could be attributed due to the relatively high surface area, ordered multi-level porosities, distinct pore structure, and designable functionalities to act as functional materials.[10] Amidst the MOF-derived metal oxides, cerium oxide (CeO_2), one of the

Centre for Nano Science and Nanotechnology, Siksha 'O' Anusnadhan (Deemed to be University), Bhubaneswar-751030, Odisha, India.
E-mail: paridakulamani@yahoo.com, kulamaniparida@soauniversity.ac.in;
Fax: +91-674-2350642; Tel: +91-674-2351777

† Electronic supplementary information (ESI) available. See DOI: https://doi.org/10.1039/d4ma00271g

affordable rare earth oxides, has been explored as a potential photocatalyst preserving some unique features such as exceptional physicochemical characteristics, admirable optical properties, readily interconvertible redox states, high photostability, and oxygen storing capacity.[11–13] Moreover, 1D CeO_2 nanorods have shown enhanced photocatalytic efficiency owing to their high length-to-diameter ratios, larger specific surface areas, and efficient charge migration within these nanoscale structures.[14] However, the practical utility of pure CeO_2 is restricted by its sluggish interfacial charge transportation, inadequate band structure, less photoabsorption capacity, back oxidation reactions, *etc.*[15] Therefore, to overcome this difficulty, it is highly reassuring to design a binary hybrid by integrating it with another potent semiconducting material to perform more productively and efficiently. Among various mechanistic insights, the direct *Z*-scheme heterojunction not only promotes efficient charge separation but also preserves the robust redox capabilities of the original photocatalysts as compared to other conventional band models.[16] For instance, Jiang *et al.* adopted an *in situ* hydrothermal approach to successfully fabricate a direct *Z*-scheme $CeO_2/ZnIn_2S_4$ heterojunction, which was effectively involved in the spatial exciton separation to increase the photocatalytic highly selective benzaldehyde oxidation and hydrogen evolution performance.[17] Similarly, Xiao *et al.* fabricated a *Z*-scheme-based $CeO_2/SnIn_4S_8$ hybrid for wastewater treatment and H_2O_2 production.[14] In this regard, a typical ternary chalcogenide, *i.e.*, magnesium indium sulfide ($MgIn_2S_4$ = MIS), might be an excellent supporting material because of its excellent physicochemical stability, optical and electrical traits, high surface area, and suitable band edge potential. Therefore, the artful fusion of MIS and C/N–CeO_2 nanorods into a heterojunction using the *Z*-scheme model could be expected to exhibit greater charge separation efficiency and photocatalytic performance.

Therefore, this work provides a comprehensive understanding of the photocatalytic H_2 and H_2O_2 evolution by *Z*-scheme-based 1D–2D, C/N–CeO_2/MIS nanocomposites. Based on our study, it can be established that the well-fitted energy level positions of constituent materials, opposite surface charges, and interfacial interaction are the main reasons for the successful fabrication of the binary hybrid. Among all, the 20% MIS loaded C/N–CeO_2 (MC-2) was found to demonstrate superior activity with production rates of 419.2 μmol h^{-1}, and 2520.4 μmol h^{-1} g^{-1} for photocatalytic H_2 and H_2O_2 evolution, respectively. Furthermore, the enhanced performance demonstrated by the best composite MC-2 could be attributed to the

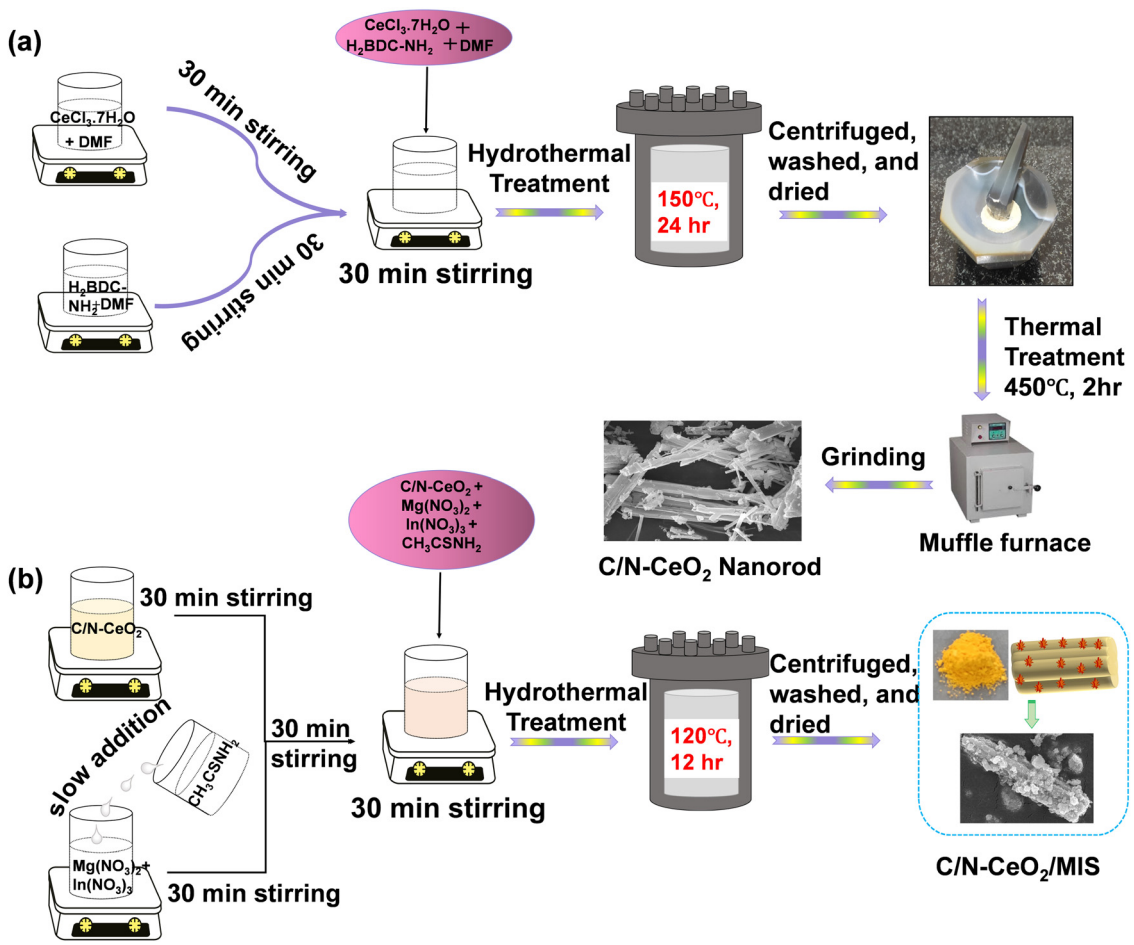

Scheme 1 Schematic of the synthesis protocol of (a) C/N–CeO_2 and (b) C/N–CeO_2/MIS photocatalysts.

greater active surface area, higher exciton lifetime, presence of OVs, and, high value of photocurrent density. These characteristics promote the spatial charge separation and transfer dynamics following the lower energy barrier reaction pathway for the rate-determining step of various reactions. Moreover, the sample showed optimum photocatalytic O_2 evolution performance. Thus, our C/N–CeO_2/MIS composites prepared following a facile synthesis technique open up a novel avenue for various photocatalytic green energy and environmental applications. The schematic of the synthesis method of pristine C/N–CeO_2 and composite MC-2 is displayed in Scheme 1, and the detailed procedure is explained in the ESI.†

2. Results and discussion

2.1 Physicochemical characterization

The crystal structure and phase purity of the as-synthesized MOF-derived C/N–CeO_2, MIS composites and Ce-MOFs were investigated by X-ray diffraction, as depicted in Fig. 1(a) and Fig. S1 (ESI†) respectively. The derived pale yellow–colored C/N–CeO_2 photocatalyst from the Ce-MOF exhibited diffraction at 2θ = 28.6°, 33.1°, 47.6°, and 56.4° assigned to the (111), (200), (220), and (311) planes, respectively, confirming the polycrystalline cubic crystal structure of C/N–CeO_2 (JCPDS card no.: 81-0792).[15] Furthermore, the distinct peaks for neat MIS at 2θ = 14.0°, 23.0°, 27.5°, 33.4°, 43.8°, 47.9°, 56.6°, 59.6°, and 66.7° were assigned to the (111), (220), (311), (400), (511), (440), (533), (444), and (731) planes, respectively, corresponding to the cubic phase of MIS (JCPDS card no. 01-070-2893).[18] However, the PXRD pattern of MC-1, MC-2, and MC-3 primarily confirmed the successful formation of the composites showing diffraction peaks at 2θ = 28.51°, 32.97°, 47.40°, and 56.32° for C/N–CeO_2 and at 2θ = 14.0° and 43.8° for MIS. Moreover, the close interaction between C/N–CeO_2 and MIS was validated through the shifting of the 2θ value to a lower angle. The high purity and crystallinity of the composites were again confirmed by the absence of any impurity peak in the XRD pattern. FTIR spectroscopy was performed for the structural elucidation of all the designed materials (Fig. 1(b)). The bands at the left end of the spectrum in between 3350 and 3500 cm^{-1} appeared due to O–H and N–H stretching. Moreover, N–H scissoring and wagging absorption peaks were cantered at 1618 cm^{-1} and 700–900 cm^{-1}, respectively.[15] Moreover, the characteristic stretching frequencies of the C–N, C–S, and S–O bonds were seen in the lower frequency region at around 1100, 730, and 1170 cm^{-1}.[18] Furthermore, Raman analysis was conducted to evaluate the microstructural crystal defects or vacancies in the materials (Fig. 1(c)).[15,19] In detail, the characteristic peak at 464 cm^{-1} was assigned to the F_{2g}-band (phonon band for CeO_8) and the peak at 273, 587.5 cm^{-1} was ascribed to the D-band (defect band) of C/N–CeO_2.[20] In addition, the vibrational modes for In–S (A_{1g}) and Mg–S (E_g) peaks of MIS were observed in the region of 200–400 cm^{-1}, displaying the existence of both the

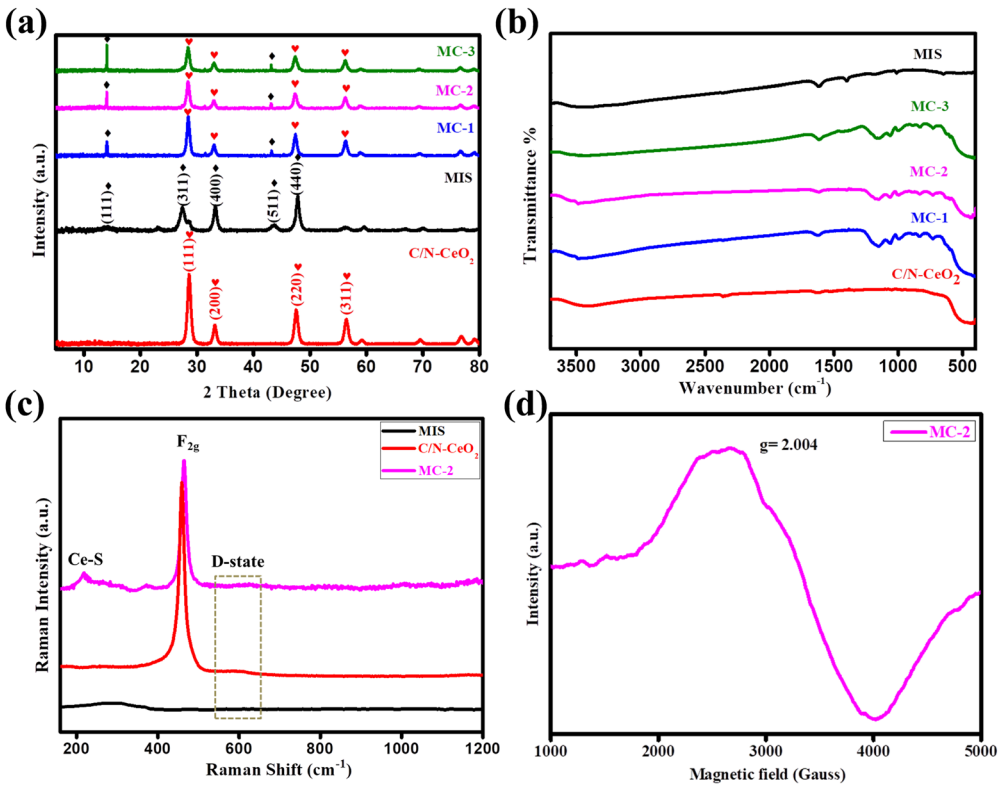

Fig. 1 (a) and (b) PXRD pattern and FT-IR spectrogram of C/N–CeO_2, MIS, MC-1, MC-2, and MC-3 composites. (c) Raman spectra of C/N–CeO_2, MIS, and MC-2. (d) EPR spectra of MC-2.

material in the composite.[21] The slight shifting in the peak position in case of MC-2 was explained by the lattice expansion and oxygen vacancy generation.[22] Besides, a noticeable peak at ~218 cm^{-1} in the composite for Ce–S bonds proved the robust chemical interaction between neat materials.[17] To further support the presence of OVs in C/N–CeO_2 (Fig. S2(a), ESI†), defect states in MIS (Fig. S2(b), ESI†), and the existence of parental property in MC-2, EPR analysis was studied. Fig. 1(d) displays the EPR spectrum of MC-2 at room temperature, for which the g value can be calculated using eqn (1):[23]

$$g = h\nu/\beta H \quad (1)$$

where h, ν, β, and H denote their usual meaning. A strong symmetrical signal at 340 mT, corresponding with g = ~1.97, was calculated for C/N–CeO_2, suggesting a model paramagnetic center, where an electron that left the OV was trapped near the surface of the Ce^{3+}/Ce^{4+} redox pair to form a Ce^{4+}–V_O–Ce^{3+} complex.[23] Similarly, a strong signal having a g value of ~2.003 was observed for MIS showing the presence of defect states.[24] Moreover, in case of MC-2, an observed signal around g = ~2.004 showed a wide resonance linewidth, which was attributed to the presence of both surface superoxide species (Ce–O_2^-) and MIS defect states.[25]

Furthermore, the specific surface area and pore size distribution of the nanocomposites were analysed by N_2 adsorption–desorption isotherm, as shown in Fig. S3(a) and (b) (ESI†). It was deduced that the adsorption process adheres to a type-IV isotherm with an H3 hysteresis loop.[15] The BET surface area of C/N–CeO_2 and MC-2 were determined to be 57.5 and 71.4 $m^2\ g^{-1}$, respectively. The much higher surface area of the binary photocatalyst compared to the neat material was due to the uniform distribution of MIS microflowers on C/N–CeO_2 nanorods, which was further confirmed by FESEM and TEM. The greater surface area of MC-2 delivered numerous active surface sites for the interaction of reactant species towards photocatalytic applications. Moreover, the peak positions in the BJH curve confirmed that the neat MIS has both micro- and mesoporous architectures, whereas neat C/N–CeO_2 and composite MC-2 showed only mesoporous structures.

To analyse the surface chemical composition and chemical state of C/N–CeO_2, MIS, and MC-2 composites, the XPS spectra

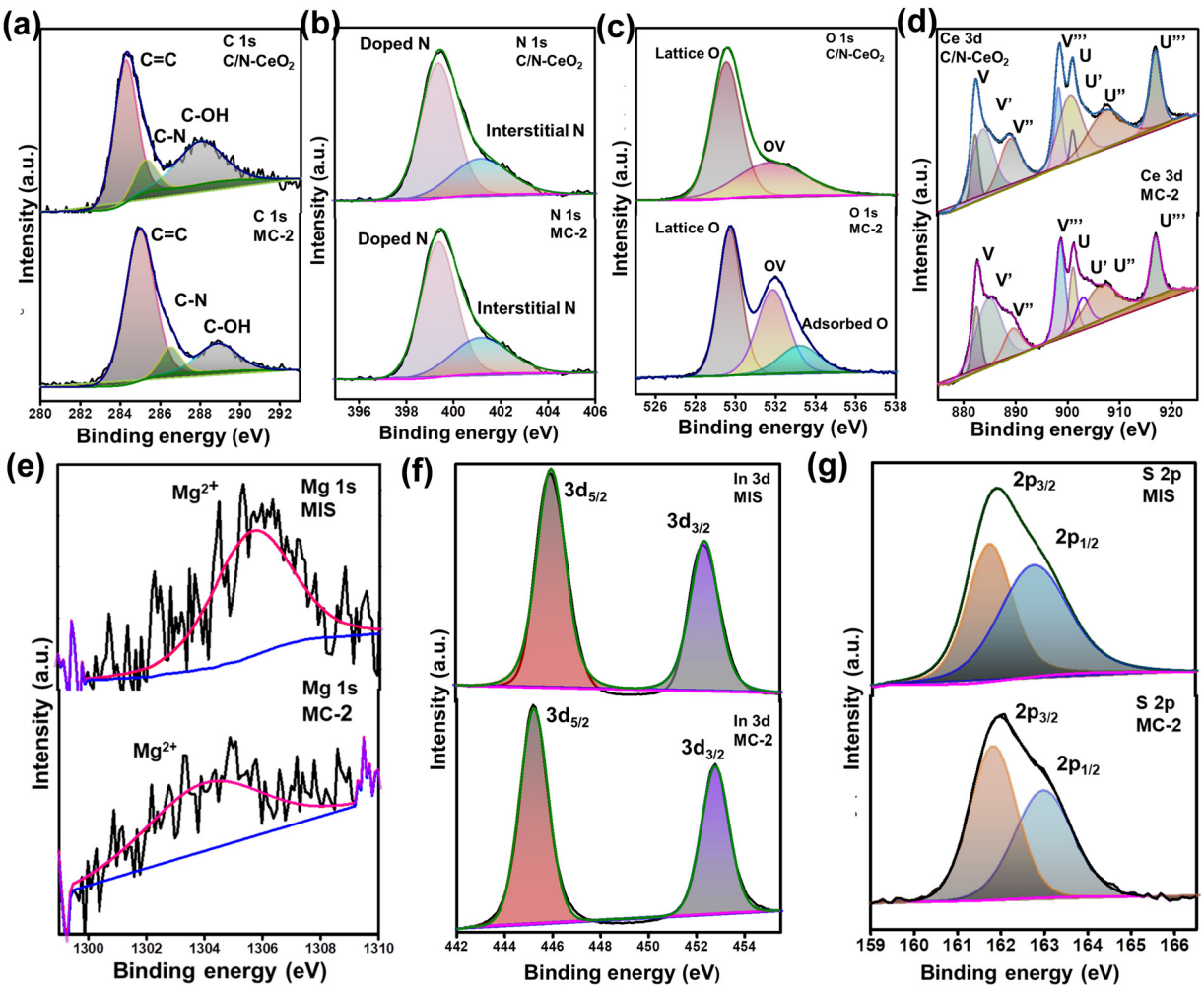

Fig. 2 High-resolution XPS spectra of C/N–CeO_2, MIS, and MC-2: (a) C 1s, (b) N 1s, (c) O 1s, (d) Ce 3d, (e) Mg 1s, (f) In 3d, and (g) S 2p.

of the samples were recorded. The XPS survey scan spectra of pristine C/N–CeO_2 and MIS are displayed in Fig. S4(a) and (b) (ESI†), which ascertain the presence of all the building elements. The XPS spectra of C 1s displayed in Fig. 2(a) exhibit three characteristic peaks at 284.85, 286.1, and 289.18 eV corresponding to the C–N, C–OH, and O=C–O groups respectively.[26] Additionally, the deconvoluted peak for the N 1s core level spectra (Fig. 2(b)) depicts the peak at 399.37 eV and 401.12 eV corresponding to the substitutional nitrogen in the O–Ce–N structure and interstitial N state in the sample.[27] The content of substitutional nonmetals was determined from the full survey spectrum of C/N–CeO_2, considering the characteristic area under the curve of C and N. The atomic percentage of carbon and nitrogen in C/N–CeO_2 was estimated to be approximately 24.50 and 6.89% respectively.[28–30] Moreover, the deconvoluted O 1s spectra of C/N–CeO_2 represent two peaks at 529.48 and 531.31 eV that correspond to C–O and oxygen vacant species (Fig. 2(c)). In MC-2, one extra peak was observed at 533.21 eV corresponding to surface-adsorbed oxygen species necessary to provide more adsorption sites for the photocatalytic reactions.[15,26] Fig. 2(d) displays the HRXPS peak of Ce 3d, which has a relatively complex structure consisting of two sets of peaks due to spin–orbit coupling between the term symbols, *i.e.*, $3d_{5/2}$ (designated as U) and $3d_{3/2}$ (designated as V). The peaks V (excluding V′) and U (excluding U′) correspond to the Ce ion in the +4 oxidation state, while V′ and U′ represent the Ce ion in the +3 oxidation state.[15,31] However, blue shifting in binding energy was observed in the case of Ce 3d peaks of MC-2, suggesting the effective interaction between the combining species. The relative concentration of Ce^{3+} to Ce^{4+} in MC-2 was approximately determined by putting the area under each peak in the Ce 3d spectrum in eqn (2), yielding an estimated value of 29%, which was around 22% in case of C/N–CeO_2.[32] This finding further supports the presence of surface defects (OVs) in MC-2, as previously proved through Raman and EPR analysis.

$$\text{Relative concentration of } Ce^{3+}(\%) = \frac{[A(Ce^{3+})]}{[A(Ce^{3+}) + A(Ce^{4+})]} \times 100 \quad (2)$$

Moreover, the Mg 1s spectrum exhibits a single peak at 1305.0 eV, which indicates the presence of Mg^{2+} in MIS, and the In 3d spectrum exhibits two peaks at 444.7 and 452.3 eV assigned to $3d_{5/2}$ and $3d_{3/2}$, indicating the presence of In^{3+} in MIS. Furthermore, the S 2p spectrum shows two broad peaks at 161.9 ($2p_{3/2}$) and 162.9 eV ($2p_{1/2}$) corresponding to S^{2-}.[3,13]

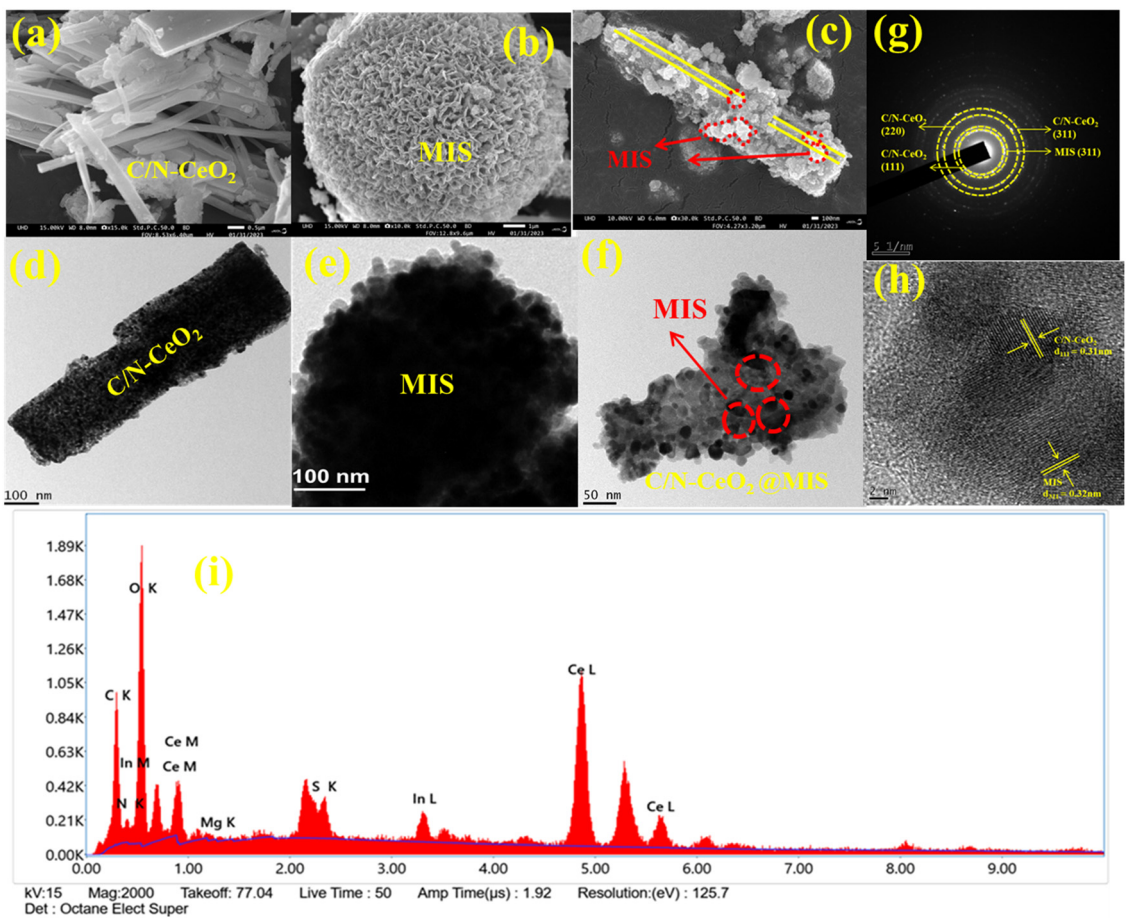

Fig. 3 (a)–(c) FESEM image of C/N–CeO_2, MIS, and MC-2. (d)–(f) TEM image of C/N–CeO_2, MIS, and MC-2. (g) SAED pattern (h) HRTEM image, and (i) EDX pattern of the MC-2 composite.

The XPS spectra analysis enabled us to find out the flow of electrons at the interface of the MC-2 heterojunction.[33] The spectra of MC-2 represent a slight positive shifting in the binding energy values for elements C, O, and Ce than neat C/N–CeO_2, whereas the peaks of Mg, In, and S showed a slight red-shifting in the binding energy value than the neat MIS. The obtained results indicate a change in the electron density of the individual materials within the MC-2 composite due to the migration of electrons from C/N–CeO_2 to MIS. Moreover, the transfer of electrons from n-type C/N–CeO_2 to n-type MIS results in an increase in electron density on the MIS surface, causing a shift in the binding energy to a lower value and *vice versa*. This change in the binding energy value confirms the successful interaction between both interacting materials and the formation of an n–n heterojunction, as a support of XRD study. Furthermore, to assist the strong interfacial interaction in the n–n heterostructure, a comprehensive investigation of surface charge analysis was conducted using zeta potential measurement (Fig. S5, ESI†). The surface potential of C/N–CeO_2 was determined to be positive, while MIS exhibited a negative potential with values of 0.6 mV and −2.2 mV, respectively.[34] All these findings support the notion of a robust interfacial interaction between C/N–CeO_2 and MIS, leading to the formation of the heterojunction.

2.2 Morphological characterizations

The morphologies and microstructure of the as-synthesized photocatalysts were analysed by FESEM and TEM. A well-defined nanorod and microflower of C/N–CeO_2 and MIS were clearly observed in the micrographs shown in Fig. 3(a) and (b). Actually, it is well known that under hydrothermal treatment, initially MIS nanoparticles are generated due to the nucleation of precursors. Subsequently with time under high-temperature and high-pressure conditions, due to the surface energies, the nanoparticles (petals) are self-assembled to form a flower-like sphere structure of MIS. Meanwhile, a distinct heterojunction composite (MC-2) is clearly shown in Fig. 3(c), which reveals that the micrometer-sized MIS petals are wrapped around many stacked nanosized rods of C/N–CeO_2, as confirmed by the TEM analysis (Fig. 3(d)–(f)). From the figure, it has been suggested that C/N–CeO_2 retains its original structure with the gathering of multiple nanorods in the composite, whereas MIS microflowers are completely exfoliated under high reaction conditions and the micrometer-sized petals/flakes are distributed on the surface of C/N–CeO_2.[35] The strong interfacial contact may speed up the transfer of photogenerated charge carriers while reducing the rate of charge recombination.[14] The concentric ring SAED pattern as shown in Fig. 3(g) suggests a polycrystalline nature of the material with the rings assigned to the (111), (220), and (311) planes of C/N–CeO_2 and the (311) plane of MIS, as confirmed by the XRD study. Additionally, the HRTEM image (Fig. 3(h)) reveals the close interface formation between C/N–CeO_2 and MIS with lattice fringes of 0.32 and 0.31 nm corresponding to (311) and (111) respectively.[15,18] Furthermore, the homogeneous distribution of MIS nanoparticles on C/N–CeO_2 was further confirmed by EDX analysis (Fig. 3(i)), and colour mapping (Fig. S6, ESI†), which has been previously reported through XPS survey spectra.

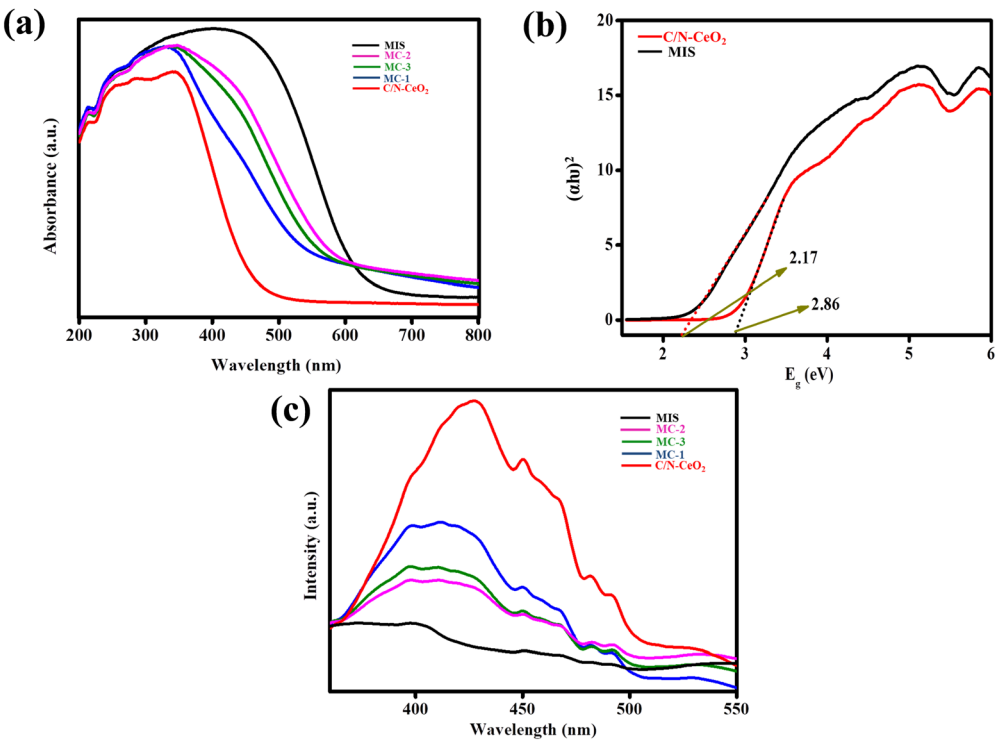

Fig. 4 (a) UV-Visible DRS spectra of C/N–CeO_2, MIS, MC-1, MC-2, and MC-3 composites. (b) Tauc plot of C/N–CeO_2 and MIS. (c) Photoluminescence (PL) spectra of C/N–CeO_2, MIS, MC-1, MC-2, and MC-3 composites.

2.3 Optical characterizations

The light capturing nature of the material played a pivotal role in photocatalytic reactions. Therefore, optical aspects such as the light absorption capacity and band gap energy of the as-fabricated materials were examined by the UV-Vis DRS study, as shown in Fig. 4(a). The spectrum of C/N–CeO_2 showed an absorption tail from UV to visible light range up to 467 nm due to the charge transfer (CT) spectra between the O^{2-} (2p) valence energy level to the Ce^{4+} (4f) conduction energy level, and the interband charge transfer because of the presence of Ce^{3+} ions.[13,36] Moreover, the composites exhibited a bathochromic shift in the visible light zone than neat C/N–CeO_2 with increased contents of MIS and MC-2 showing maximum absorption. The enriched light harvesting ability of the binuclear heterostructure with the optimal content of excellent visible light absorbing MIS on C/N–CeO_2 revealed the entrenched design of the heterostructure between the two neat materials. Furthermore, the Tauc plot was employed to evaluate the band gap of pristine materials by plotting the graph between the energy and absorption value using eqn (3):[37]

$$Ahv = A\,(hv - E_g)^n \quad (3)$$

where E_g, A, h, ν, and α correspond to their usual meaning, $n = 2$, representing the direct semiconductor nature of the two materials. Using the equation, the direct band gap of C/N–CeO_2, and MIS was calculated to be 2.86 and 2.17 eV respectively (Fig. 4(b)). Therefore, MC-2 nanohybrid was expected to exhibit enhanced light absorption, which would contribute to more effective use of the energy from visible light than the neat materials. Moreover, to study the exciton separation, transformation, and migration in order to produce the blueprint of a photocatalytic reaction pathway, photoluminescence (PL) spectroscopy was studied under ambient conditions. As shown in Fig. 4(c), the PL peaks at around 373 nm, 429 nm, and 540 nm were probably related to surface states, OV, and self-trapping excitation in C/N–CeO_2, respectively.[15] The PL peak of analysed composites was recorded at λ_{ex} = 360 nm, displaying a remarkable decrease in the emission peak, and the lowest PL peak intensity was observed for MC-2. The PL spectrum highlights the nature of the plot, which signifies the following order of charge separation: C/N–CeO_2 < MC-1 < MC-3 < MC-2 < MIS. Consequently, the findings suggested that in MC-2, photoexcited electrons and holes are efficiently separated, resulting in a higher concentration of excitons at their respective energy levels.[36] This enhanced separation facilitates the effective execution of photocatalytic reactions. Moreover, the minimized PL intensity of MIS signifies the low photo-excitation efficiency with respect to other synthesized materials. Further, to extend the above discussion, time-resolved photoluminescence (TRPL) analysis was performed (Fig. S7, ESI†) to calculate the average lifetime of photo-excited charge carriers, which was fitted to equation (4):

$$A + B1\exp(-t/\tau 1) \quad (4)$$

where all symbols denote their usual meaning.[38] As can be interpreted, the TRPL peak of the MC-2 composite displayed a longer average fluorescence lifetime (τ = 0.42 ns) than that of neat C/N–CeO_2 (τ = 0.27 ns) and MIS (τ = 0.23 ns), providing

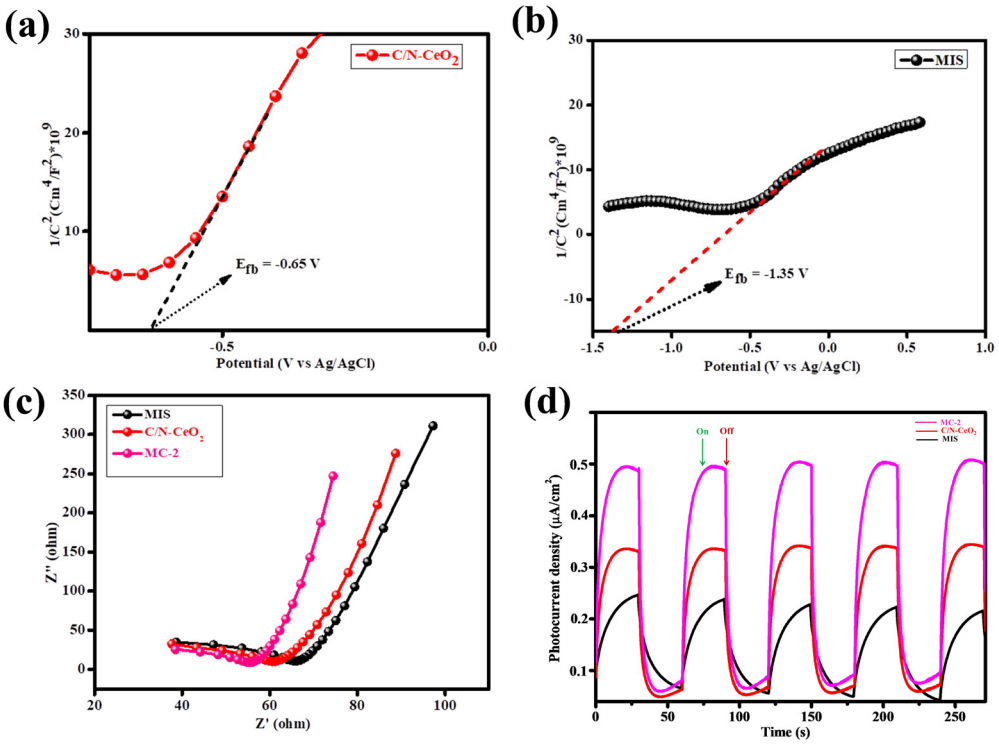

Fig. 5 (a) Mott–Schottky plot of C/N–CeO_2. (b) Mott–Schottky plot of MIS. (c) and (d) EIS and photocurrent plot of C/N–CeO_2, MIS, and MC-2 respectively.

evidence for the accelerated transportation of electrons from electron-rich C/N–CeO_2 to electron-deficient MIS through the heterojunction formed between them.

2.4 Electrochemical characterizations

To acquire the fundamental grasp on the nature of semiconducting materials and flat band potential values, MS analysis was performed for C/N–CeO_2 and MIS. Fig. 5(a) and (b) represents the MS plot of C/N–CeO_2 and MIS plotted for $1/c^2$ *vs.* potential (V) under ambient conditions at an externally applied frequency of 500 Hz.[15,18] By extrapolating the $1/c^2$ value along the *X*-axis, the flat band potential was calculated having values as −0.65 V and −1.35 V for C/N–CeO_2 and MIS, respectively. Meanwhile, the determined positive slop of the plot demonstrates the n-type characteristics of both the neat materials. In addition, the electrode potential ($E_{Ag/AgCl}$) could be converted into the NHE scale at pH = 7 using eqn (5):[39]

$$E_{(NHE)} = E_{Ag/AgCl} + E^0_{Ag/AgCl} - 0.0591(7 - pH) \quad (5)$$

$E^0_{Ag/AgCl}$ = 0.197 V at 25 °C. By using the above-mentioned equation, the Fermi level position of C/N–CeO_2 and MIS was obtained to be −0.46 eV, and −1.16 eV respectively. The generalised concept as per literature study conveyed that, for n-type semiconductors, the Fermi energy level *vs.* NHE lies at about 0.1–0.3 eV below the CB position. Therefore, by considering 0.1 eV variations, the CB of C/N–CeO_2 and MIS were found to be −0.56 and −1.26 eV, respectively. Again, combining the band gap value from the Kubleka-Munk function with the CB potential, the VB values of C/N–CeO_2 and MIS were calculated to be 2.3 eV and 0.91 eV, respectively. In addition, ultraviolet photoelectron spectroscopy (UPS) analysis was performed using HeI emission ($h\nu$ = 21.22 eV) as the light source to determine the ionization potential (equal to E_{VB}) and work function (φ) of C/N–CeO_2 and MIS.[40] As illustrated in Fig. S8 (ESI†), the cutoff energies (E_{cutoff}) of C/N–CeO_2 and MIS are 14.84 and 15.50 eV, respectively, and their corresponding onset energies (E_{onset}) are 0.93 and 0.33 eV, respectively. Using eqn (6), the E_{VB} values of C/N–CeO_2 and MIS were calculated to be 7.3 and 6.0 eV, which were further converted to be 2.8 and 1.6 V according to the reference standard for which 0 V *vs.* RHE equals −4.44 eV. The E_{VB} results are close to the above-calculated VB potentials. Moreover, the φ values for C/N–CeO_2 and MIS were calculated using eqn (7) to be 6.38 and 5.72 eV respectively:[41,42]

$$E_{VB} = 21.22 - (E_{cutoff} - E_{onset}) \quad (6)$$

$$\varphi = 21.22 - E_{cutoff} \quad (7)$$

In addition to PL analysis, the photogenerated exciton separation and transfer process were further investigated using EIS under light conditions consisting of two main regions. The frequency-dependent exciton transfer mechanism of the as-synthesised materials was presented by the Nyquist plot measured within the scanning window of 10^2 to 10^5 Hz and at an amplitude of 0.025 V.[38] The EIS spectra of all the synthesised materials are depicted in Fig. 5(c). It was observed that in the case of MC-2, a smaller arc radius with a straighter conductive loop was obtained, suggesting a superior charge transfer mechanism.[43] The results from the above investigation showed good relevance with the photoluminescence and photocatalysis studies.

To collect more data about the exciton segregation efficacy, the transient photocurrent of the as-synthesized materials was studied.[3,15] The separation effectiveness of photogenerated electrons and holes was closely associated with the photocurrent density of the photocatalysts. From the graph (Fig. 5(d)) the photocurrent densities for neat C/N–CeO_2, and MIS were found to be 0.33, and 0.24 μA cm^{-2}, suggesting the poor segregation ability of the e^-/h^+ pairs. Nevertheless, the MC-2 composite demonstrated the highest photocurrent value, reaching 0.53 μA cm^{-2}, which was approximately 1.6 times greater than that of neat C/N–CeO_2 and 2.2 times greater than that of MIS. This improvement can be attributed to the enhanced migration of charge carriers at the interface resulting from the established heterostructure between the n-type C/N–CeO_2 and MIS.

3. Photocatalytic activity and stability of the as-synthesized photocatalysts

The catalytic activity of the designed materials was tested towards light-induced hydrogen evolution reactions. Pristine C/N–CeO_2 and MIS exhibited minimal HER activity owing to the

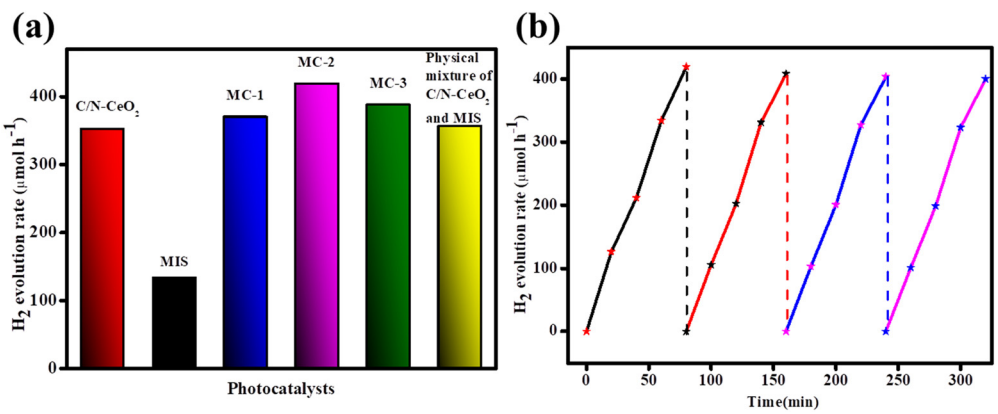

Fig. 6 (a) H_2 evolution activity of C/N–CeO_2, MIS, MC-1, MC-2, and MC-3 composites. (b) Reusability test for MC-2.

narrow light absorption range and faster carrier recombination rate. However, an accelerated HER activity was observed for binary composites (MC-1, MC-2, and MC-3). The observed activity order was found to be 419.2 μmol h^{-1} with an apparent conversion efficiency (ACE) of 6.73% for MC-2, 370.18 μmol h^{-1} for MC-1 and 388.02 μmol h^{-1} for MC-3 (Fig. 6(a)). The enhanced catalytic activity of MC-2 is attributed to the easily convertible oxidation state (Ce^{3+}/Ce^{4+}), greater exciton lifetime, surface OVs, narrow bandgap, *etc.*[31] Moreover, the best catalyst (MC-2) has shown excellent photostability confirmed from the reusability test depicted in Fig. 6(b).

Further, the photocatalytic H_2O_2 production of the designed catalysts was estimated *via* a $2e^-$ oxygen reduction process, and the results are depicted in Fig. 7(a). It was evidenced that both the neat MIS and C/N–CeO_2 exhibited minimal catalytic activity, *i.e.* 545 and 1342.85 μmol h^{-1} g^{-1} owing to faster carrier recombination and narrow light absorption tendency respectively. However, enhanced catalytic activity was encountered for composite materials compared to the pristine material. The photocatalytic H_2O_2 production for MC-1, MC-2, and MC-3 was determined to be 2115.2, 2520.4, and 2383.0 μmol h^{-1} g^{-1} respectively. The optimum MIS content in MC-2 provides many surface-active sites for appropriate O_2 adsorption that accelerates the activity. The effect of different sacrificial agents (methanol, ethanol, and isopropanol) as proton donors was investigated as excess proton concentration slow down the consumption of holes by alcohol oxidation. Moreover, the result followed the sequence: IPA (2520.4 μmol h^{-1} g^{-1}) > ethanol (1884.3 μmol h^{-1} g^{-1}) > methanol (2067.6 μmol h^{-1} g^{-1}), as shown in Fig. 7(b). Furthermore, in order to examine the effect of atmospheric condition, the reaction was carried out under O_2 and Ar atmospheres, and the result is depicted in Fig. 7(c). A reasonable rate of H_2O_2 production was obtained by purging O_2 through the reaction mixture, which signified the indispensable role of oxygen flow for photocatalytic H_2O_2 production. Additionally, the solar to chemical conversion efficiency (SCC %) of the MC-2 composite was calculated to be 0.16% and the detailed calculation was provided in the ESI.† The recycle test graph for the MC-2 composite (Fig. 7(d)) showed no appreciable decrease in H_2O_2 evolution capacity after four repeated runs, indicating the long-term photostability of the catalyst.

Photon-assisted water oxidation is regarded as a challenge, and it kinetically slows down the reaction due to its involvement in a four-electron-proton coupling process.[15] In this regard, the as-synthesized photocatalysts, *i.e.*, C/N–CeO_2, MIS, and MC-2, were applied towards photocatalytic O_2 evolution under light irradiation. The obtained results are demonstrated in Fig. 8(a), which showed the maximum O_2 evolution rate of 210.09 μmol h^{-1} with an ACE of 3.37% for the MC-2 photocatalyst. The attributed result was supported by the PL, TRPL, and EIS plot, demonstrating the effective charge separation and a longer lifetime of excitons in the case of MC-2 nanohybrids. Furthermore, in the context of investigating the water oxidation reaction, defect-oriented materials hold specific interest due to the formation of intermediate O-atom produced during the cleavage of attached water molecules.[44] Again, the possibility of back reaction and the probability of following high energetic reaction pathways get reduced in the case of defect-oriented materials, which signifies the superiority of MOF-derived vacancy-rich C/N–CeO_2 over conventional CeO_2.[11,15] Furthermore,

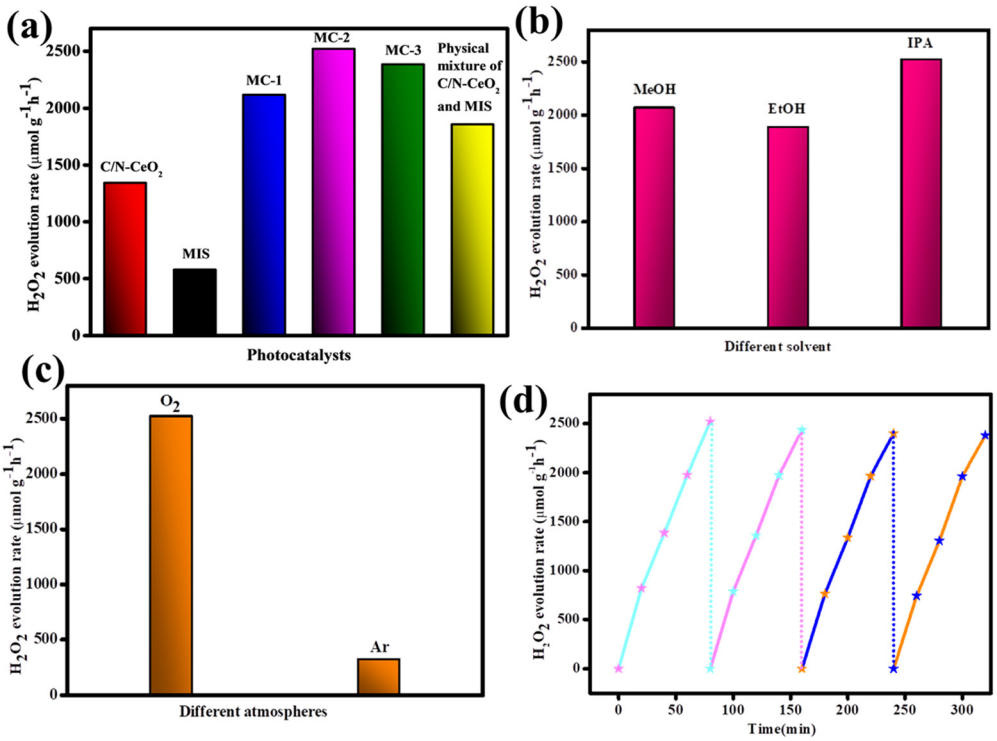

Fig. 7 (a) H_2O_2 evolution rate of different catalysts. (b) Scavenging test. (c) Different gaseous atmospheres. (d) Reusability test for the MC-2 photocatalyst.

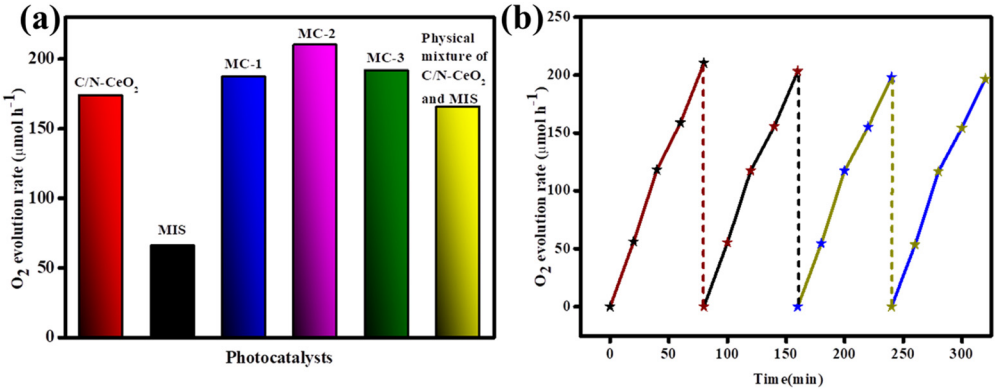

Fig. 8 (a) O_2 evolution plot of C/N–CeO_2, MIS, MC-1, MC-2, and MC-3 composites. (b) Reusability test for O_2 evolution using the MC-2 photocatalyst.

the photo-stability of MC-2 is demonstrated in Fig. 8(b), which found very minute reduction in activity up to four consecutive cycles. In addition, the XRD spectrum of the used MC-2 photocatalyst is displayed in Fig. S12 (ESI†), which exhibits a little intensity loss and good structural stability of the photocatalyst. A comparative table of each case of activity is provided in the ESI† (Tables S5, S6, and S7 for H_2, O_2, and H_2O_2 evolution rate, respectively) for better correlation with the activity of other metal oxide–based photocatalysts.

4. Mechanism based on the *Z*-scheme charge dynamics

The probable mechanistic pathway of the C/N–CeO_2/MIS binary heterojunction towards photocatalytic applications is depicted in Scheme 2, which displays the possibility of two kinds of flawless charge flows, *i.e.*, type II (Scheme 2a) and *Z*-scheme (Scheme 2b). Under UV-Visible light illumination, the photo-induced electrons and holes were produced and accumulated at the respective CB of MIS (CB_{MIS}) and the VB of C/N–CeO_2 ($VB_{C/N-CeO_2}$). Nevertheless, the traditional type II heterojunction (Scheme 2a) band alignment for the C/N–CeO_2/MIS hybrid will be feasible if there is a drastic reduction in the •OH formation, as the VB potential of MIS (VB_{MIS} = 0.91 V) is less positive than 1.99 V.[45] However, the presence of •OH and $•O_2^-$ has already been established by the TA and NBT trapping test displayed in Fig. S10(a) and (b) (ESI†). Therefore, a reasonable *Z*-scheme mechanism was put forward, as shown in Scheme 2b, to authenticate the assumptions for the successful occurrence of photocatalytic reactions at the respective surface sites.[13] Moreover, the UPS study of C/N–CeO_2 showed a larger φ value (6.38 eV) and a

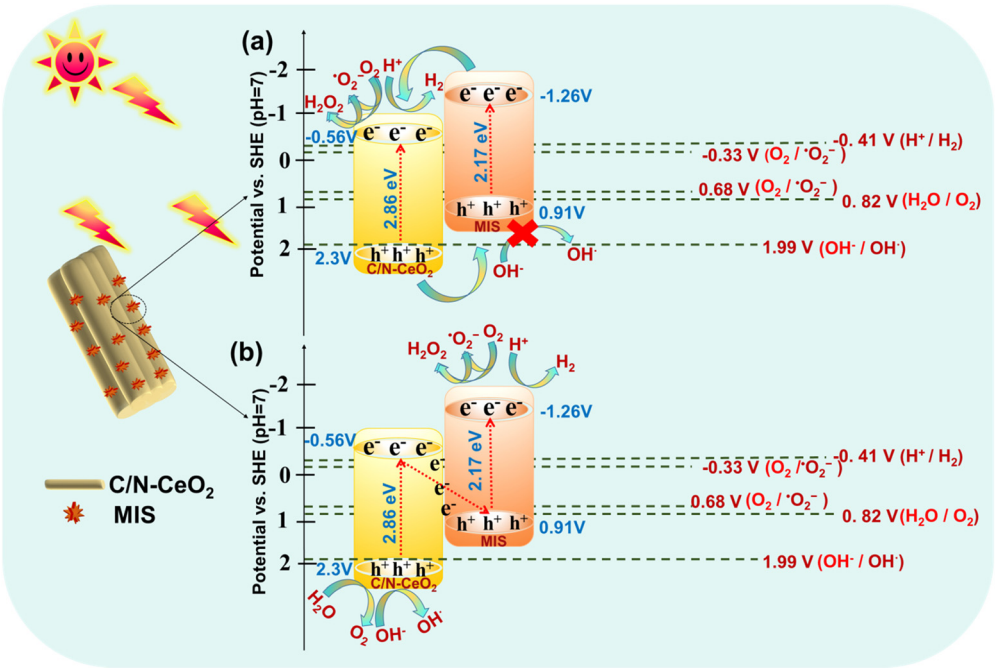

Scheme 2 Schematic of the probable charge transfer mechanism in (a) type II and (b) *Z*-scheme heterojunctions and the generation of •OH radicals in the *Z*-scheme heterojunction rather than the type II heterojunction.

lower Fermi level before contact, while MIS exhibited a smaller φ value (5.72 eV) and a higher Fermi level (Scheme 3a), and their E_f reached balance instantly once the heterojunction was formed *via* the impulsive surge of electron flow from MIS to C/N–CeO_2. As a result, MIS became positively charged by donating an electron, whereas C/N–CeO_2 became negatively charged by accepting the electron. This type of electronic transition leads to creation of an internal electric field at the interfacial space region, which induces band-bending and promotes charge carrier segregation.[33,46] Upon UV-Vis light illumination, in the case of C/N–CeO_2, some of the excited carriers immediately migrated from the VB to the sub-band of OVs and some charge from the CB also get trapped in the same. In addition, at the electrode interface, the photo-excited electrons at $CB_{C/N-CeO_2}$ can effectively unite with the holes at VB_{MIS}, which results from the availability of highly reducing electrons at CB_{MIS} and highly oxidizing holes at $VB_{C/N-CeO_2}$ to carry out the catalytic reactions. In this process, OVs behave as a hub that trap electrons and also as a charge mediator creating a carrier-transfer bridge between the $CB_{C/N-CeO_2}$ and the VB_{MIS}, which accelerate the transfer and separation of remaining charge carriers at the *Z*-scheme junction (Scheme 3b).[41]

Furthermore, the accumulated electrons at the CB_{MIS} react with supplied O_2 to form $^{\bullet}O_2^-$, while the photo-induced holes at the $VB_{C/N-CeO_2}$ hydroxide ion form $^{\bullet}OH$. Furthermore, $^{\bullet}O_2^-$ reacts with H^+ from the reaction medium to produce H_2O_2, while the produced $^{\bullet}OH$ can combine with another species of its own to form H_2O_2 at the $VB_{C/N-CeO_2}$. Additionally, to get further information regarding the reactive oxygen species (ROS) involved in the mechanism pathway, active species experiments were performed. Different quenchers such as *p*-benzoquinone (*p*-BQ), isopropyl alcohol (IPA), citric acid (CA), and dimethyl sulfoxide (DMSO) were used for trapping $^{\bullet}O_2^-$, $^{\bullet}OH$, h^+, and e^- respectively (Fig. S9, ESI†). According to the trapping experiment test, a substantial reduction in the production efficiency of H_2O_2 was observed while using DMSO and *p*-BQ as scavenging agents, which demonstrates the principal role of e^- and $^{\bullet}O_2^-$ for the reduction of O_2 *via* the 2-electron single-step and 1-electron two-step processes. However, the production of H_2O_2 was also affected using IPA and CA as scavenging agents, displaying the moderate involvement of $^{\bullet}OH$ and h^+ in the reaction.

Moreover, the DMPO-ESR spin-trap technique was implemented to confirm the presence of reactive radicals, *i.e.*, $^{\bullet}O_2^-$ and $^{\bullet}OH$, and to further verify the precision of the proposed *Z*-scheme charge dynamics. In this experiment, DMPO was utilized as a radical generator to seize $^{\bullet}O_2^-$ and $^{\bullet}OH$ in methanol and water solutions, respectively. From Fig. 9(a) and (b), we see that no signals of DMPO-$^{\bullet}O_2^-$ and DMPO-$^{\bullet}OH$ were observed using the MC-2 photocatalyst in the darkness. However, stronger characteristic peaks for DMPO-$^{\bullet}O_2^-$ and DMPO-$^{\bullet}OH$ were detected over the MC-2 photocatalyst under UV-visible light irradiation, displaying that the photogenerated electrons were mainly accumulated on the CB_{MIS} (as electrons at $CB_{C/N-CeO_2}$ immediately united with holes in VB_{MIS}) and the holes mainly stayed in the $VB_{C/N-CeO_2}$ (as VB_{MIS} is 0.91 eV $\ll$ 1.99 eV). Therefore, based on the above discussion, a direct *Z*-scheme photocatalytic mechanism was effectively elucidated.[16,47]

Additionally, the diminished PL intensity and prolonged lifetime of excitons indicate a faster interfacial charge transfer and more efficient charge separation between C/N–CeO_2 and MIS, which promotes charge transfer to the reactive surface sites of the MC-2 photocatalyst. The photocurrent and EIS study also appraise the photocatalysts' ability to display enhanced photocurrent upon light irradiation and good transfer of photoproduced charge carriers, respectively. Moreover, the

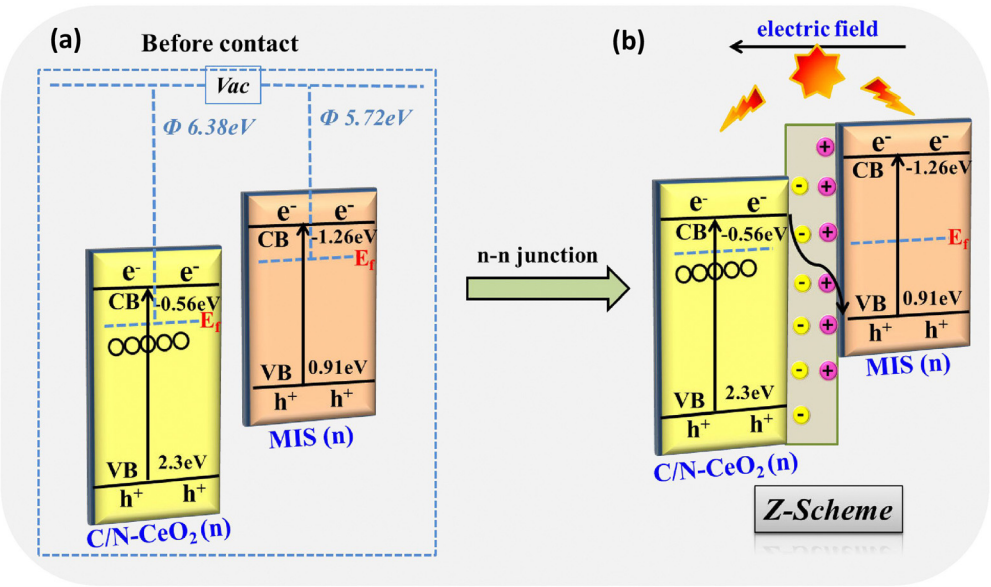

Scheme 3 (a) Work function of C/N–CeO_2 and MIS before interaction. (b) Electric field and band-edge bending at the interfacial space after contact and *Z*-scheme charge dynamics between C/N–CeO_2 and MIS.

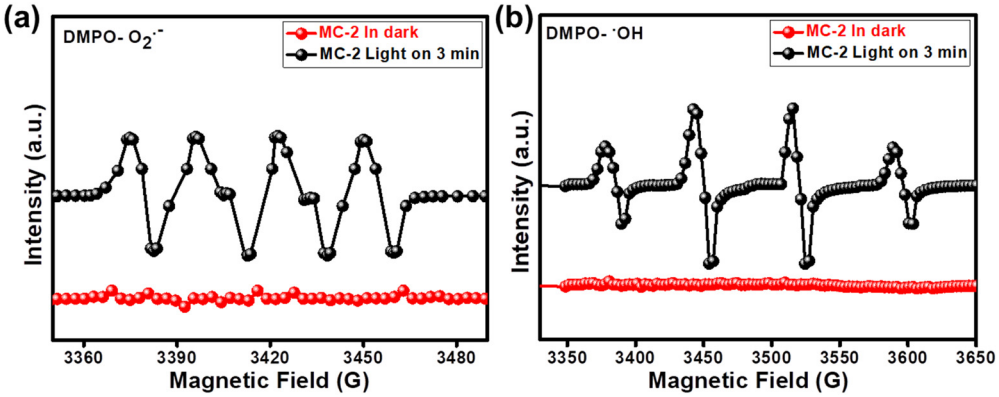

Fig. 9 Spin trapping ESR spectra of MC-2 under dark and light conditions for (a) DMPO-$^{\bullet}O_2^-$ and (b) DMPO-$^{\bullet}$OH.

EIS Nyquist plot of MC-2 revealed a smaller semicircle, indicating the fastest interfacial electron transfer ability, and thus it exhibited the highest photocatalytic activity, as discussed in the photocatalytic activity section.

H_2O_2 evolution reaction steps:

$$C/N\text{–}CeO_2/MIS + h\nu \rightarrow C/N\text{–}CeO_2{}^*/MIS^* (e_{CB}^- + h_{VB}^+) \quad (i)$$

$$C/N\text{–}CeO_2{}^*/MIS^* (e_{CB}^- + h_{VB}^+) \rightarrow C/N\text{–}CeO_2 (h_{VB}^+)/MIS (e_{CB}^-) \quad (ii)$$

$$MIS (e_{CB}^-) + O_2 \rightarrow {}^{\bullet}O_2^- \quad (iii)$$

$$MIS (e_{CB}^-) + {}^{\bullet}O_2^- + 2H^+ \rightarrow H_2O_2 \quad (iv)$$

$$H_2O \rightarrow H^+ + OH^- \quad (v)$$

$$C/N\text{–}CeO_2 (h_{VB}^+) + OH^- \rightarrow OH^{\bullet} \quad (vi)$$

$$OH^{\bullet} + OH^{\bullet} \rightarrow H_2O_2 \quad (vii)$$

H_2 evolution reaction steps:

$$C/N\text{–}CeO_2/MIS + h\nu \rightarrow C/N\text{–}CeO_2{}^*/MIS^* (e_{CB}^- + h_{VB}^+) \quad (viii)$$

$$C/N\text{–}CeO_2{}^*/MIS^* (e_{CB}^- + h_{VB}^+) \rightarrow C/N\text{–}CeO_2 (h_{VB}^+)/MIS (e_{CB}^-) \quad (ix)$$

$$H_2O \rightarrow H^+ + OH^- \quad (x)$$

$$MIS (e_{CB}^-) + 2H^+ \rightarrow H_2 \quad (xi)$$

5. Conclusion

In this work, an MIS micropetal–decorated C/N-doped MOF-derived CeO_2 photocatalyst has been constructed by a facile *in situ* hydrothermal method. The accelerated photocatalytic activity can be ascribed to the following reasons:

■ The introduction of an MIS microflower as a support material enables the creation of a high surface area, facilitating the generation of 1D/2D contact and a significant number of active sites on the surface of C/N–CeO_2.

■ Surface OVs are responsible for broadening and intensifying light absorption, modifying surface properties to lower surface-adsorption barriers, and serving as trapping sites for excited electrons, thus impeding the carrier recombination and segregation of charge carriers.

■ The robust interaction between C/N–CeO_2 and MIS enables inhibiting the further decomposition of H_2O_2 into $^{\bullet}$OH.

■ This can also potentially extend the average fluorescence lifetime of photoinduced carriers, resulting in improved efficacy in their separation.

■ The opposite surface charges serve as evidence for the synergistic coupling between the two pristine materials, leading to the design of an appropriate *Z*-scheme system verified *via* the UPS study and ESR analysis.

In this work, we provided new insights into the design and fabrication of a novel *Z*-scheme heterojunction, which can be potentially extended to the synthesis of other metal oxide–based systems using suitable MOF templates towards various photocatalytic applications.

Conflicts of interest

The authors declare that they have no known competing financial interests or personal relationships that could have appeared to influence the work reported in this paper.

Acknowledgements

S 'O' A Deemed to be University, Bhubaneswar, Odisha's management and staff are thankfully acknowledged for their constant support and encouragement in this work.

References

1 H. I. Kim, Y. Choi, S. Hu, W. Choi and J. H. Kim, *Appl. Catal., B*, 2018, **229**, 121–129.
2 H. Hou, X. Zeng and X. Zhang, *Angew. Chem., Int. Ed.*, 2020, **59**, 17356–17376.
3 L. Acharya, G. Swain, B. P. Mishra, R. Acharya and K. Parida, *ACS Appl. Energy Mater.*, 2022, **5**, 2838–2852.
4 H. Xu, S. Yang, J. Huang and H. Jiang, *ACS Catal.*, 2018, **8**, 11615–11621.

5 X. Liu, L. Liu, Z. Yao, Z. Yang and H. Xu, *Colloids Surf., A*, 2020, **599**, 124869.
6 Y. Quan, G. Wang and Z. Jin, *ACS Appl. Energy Mater.*, 2021, **4**, 8550–8562.
7 S. Subudhi, S. Mansingh, S. P. Tripathy, A. Mohanty, P. Mohapatra, D. Rath and K. Parida, *Catal. Sci. Technol.*, 2019, **9**, 6585–6597.
8 S. P. Tripathy, S. Subudhi, A. Ray, P. Behera, G. Swain, M. Chakraborty and K. Parida, *Langmuir*, 2023, **39**, 7294–7306.
9 Y. Wang, Y. Liu, H. Wang, W. Liu, Y. Li, J. Zhang, H. Hou and J. Yang, *ACS Appl. Energy Mater.*, 2019, **2**, 2063–2071.
10 P. Li, M. Zhang, X. Li, C. Wang, R. Wang, B. Wang and H. Yan, *J. Mater. Sci.*, 2020, **55**, 15930–15944.
11 S. Maiti, T. Dhawa, A. K. Mallik and S. Mahanty, *Sustainable Energy Fuels*, 2017, **1**, 288–298.
12 R. Fiorenza, S. Sciré, L. D'Urso, G. Compagnini, M. Bellardita and L. Palmisano, *Int. J. Hydrogen Energy*, 2019, **44**, 14796–14807.
13 S. Zhao, S. Li, Y. Long, X. Shen, Z. Zhao, Q. Wei, S. Wang, Z. Zhang, X. Zhang and Z. Zhang, *Chemosphere*, 2021, **280**, 130637.
14 Y. Xiao, Y. Tao, Y. Jiang, J. Wang, W. Zhang, Y. Liu, J. Zhang, X. Wu and Z. Liu, *Sep. Purif. Technol.*, 2023, **304**, 122385.
15 S. Mansingh, S. Subudhi, S. Sultana, G. Swain and K. Parida, *ACS Appl. Nano Mater.*, 2021, **4**, 9635–9652.
16 P. Mishra, A. Behera, D. Kandi, S. Ratha and K. Parida, *Inorg. Chem.*, 2020, **59**, 4255–4272.
17 C. Jiang, H. Wang, Y. Wang and H. Ji, *Appl. Catal., B*, 2020, **277**, 119235.
18 G. Swain, S. Sultana and K. Parida, *ACS Sustainable Chem. Eng.*, 2020, **8**, 4848–4862.
19 C. Schilling, A. Hofmann, C. Hess and M. V. Ganduglia-Pirovano, *J. Phys. Chem. C*, 2017, **121**, 20834–20849.
20 Y. Pu, Y. Luo, X. Wei, J. Sun, L. Li, W. Zou and L. Dong, *Appl. Catal., B*, 2019, **254**, 580–586.
21 S. Subudhi, G. Swain, S. P. Tripathy and K. Parida, *Inorg. Chem.*, 2020, **59**, 9824–9837.
22 C. Zeynep, S. Akdogan, B. Gokcal, M. Polat, K. O. Hamaloglu, C. Kip and A. Tuncel, *ACS Sustainable Chem. Eng.*, 2022, **10**, 9492–9505.
23 R. M. Rakhmatullin, V. V. Semashko, S. L. Korableva, A. G. Kiiamov, A. A. Rodionov, R. Tschaggelar, J. A. Van Bokhoven and C. Paun, *Mater. Chem. Phys.*, 2018, **219**, 251–257.
24 J. R. González, R. Alcántara, J. L. Tirado, A. J. Fielding and R. A. W. Dryfe, *Chem. Mater.*, 2017, **29**, 5886–5895.
25 W. Wang, Q. Zhu, F. Qin, Q. Dai and X. Wang, *Chem. Eng. J.*, 2018, **333**, 226–239.
26 S. P. Tripathy, S. Subudhi, A. Ray, P. Behera, A. Bhaumik and K. Parida, *Langmuir*, 2022, **38**, 1766–1780.
27 X. Cheng, X. Yu and Z. Xing, *Appl. Surf. Sci.*, 2012, **258**, 3244–3248.
28 D. Szczuko, J. Werner, S. Oswald, G. Behr and K. Wetzig, *Appl. Surf. Sci.*, 2001, **179**, 1–6.
29 A. G. Shard, *J. Vac. Sci. Technol. A*, 2020, **38**, 041201.
30 E. Paparazzo, *Mater. Res. Bull.*, 2011, **46**, 323–326.
31 S. Payra and S. Roy, *J. Phys. Chem. C*, 2021, **125**, 8497–8507.
32 C. Yang, J. Yang, X. Duan, G. Hu, Q. Liu, S. Ren, J. Li and M. Kong, *Adv. Powder Technol.*, 2020, **31**, 4072–4081.
33 S. Subudhi, G. Swain, S. P. Tripathy and K. Parida, *Inorg. Chem.*, 2020, **59**, 9824–9837.
34 S. Hussain, F. Al-Nsour, A. B. Rice, J. Marshburn, B. Yingling, Z. Ji, J. I. Zink, N. J. Walker and S. Garantziotis, *ACS Nano*, 2012, **6**, 5820–5829.
35 G. Swain, S. Sultana, J. Moma and K. Parida, *Inorg. Chem.*, 2018, **57**, 10059–10071.
36 B. Deng, H. Song, K. Peng, Q. Li and J. Ye, *Appl. Catal., B*, 2021, **298**, 120519.
37 T. Inoue, A. Fujishima, S. Konishi and K. Honda, *Nature*, 1979, **277**, 637–638.
38 A. Ray, S. Subudhi, S. P. Tripathy, L. Acharya and K. Parida, *Adv. Mater. Interfaces*, 2022, **9**, 2201440.
39 S. Subudhi, D. Rath and K. M. Parida, *Catal. Sci. Technol.*, 2018, **8**, 679–696.
40 W. Chun, A. Ishikawa, H. Fujisawa, T. Takata, J. N. Kondo, M. Hara, M. Kawai, Y. Matsumoto and K. Domen, *J. Phys. Chem. B*, 2003, **5**, 1798–1803.
41 J. Hu, C. Chen, Y. Zheng, G. Zhang, C. Guo and C. M. Li, *Small*, 2020, **16**, 2002988.
42 C. Chen, J. Hu, X. Yang, T. Yang, J. Qu, C. Guo and C. M. Li, *ACS Appl. Mater. Interfaces*, 2021, **13**, 20162–20173.
43 A. Ray, S. Sultana, S. P. Tripathy and K. Parida, *ACS Sustainable Chem. Eng.*, 2021, **9**, 6305–6317.
44 V. I. Markoulaki, I. T. Papadas, I. Kornarakis and G. S. Armatas, *Nanomaterials*, 2015, **5**, 1971–1984.
45 S. Wang, B. Zhu, M. Liu, L. Zhang, J. Yu and M. Zhou, *Appl. Catal., B*, 2019, **243**, 19–26.
46 K. K. Das, S. Mansingh, D. P. Sahoo, R. Mohanty and K. Parida, *New J. Chem.*, 2022, 5785–5798.
47 B. Ng, L. K. Putri, X. Y. Kong, Y. W. Teh and P. Pasbakhsh, *Adv. Sci.*, 2020, **7**, 1903171.